

Photophysics of O-band and transition metal color centers in monolithic silicon for quantum communications

Murat Can Sarihan*,¹ Jiahui Huang*,¹ Jin Ho Kang,¹ Cody Fan,¹ Wei Liu,¹ Khalifa M. Azizur-Rahman,^{1,2} Baolai Liang,¹ and Chee Wei Wong¹

¹*Department of Electrical and Computer Engineering, University of California, Los Angeles, California, USA*

²*Center for Integrated Nanotechnologies, Sandia National Laboratories, Albuquerque, New Mexico, USA*

Color centers at the low-dispersion O-band wavelengths are an essential resource for long-lifetime quantum network nodes toward memory-assisted quantum communications using energy-time entanglement. In this work, we explore the process of developing T centers and transition-metal color center defects for high-fidelity spin-photon interfaces with less host-related decoherence pathways, while examining the photoluminescence dynamics. Our process resulted in a T-center ensemble with minimum lattice disturbance with photophysical properties closer to ab initio predictions and host lattice. $^{63}\text{Cu}_n^m$ related doublet emission around 1312 nm close to the zero-dispersion wavelength is examined. A magnetic-field induced broadening by 25% under 0.5 T is observed, which can be related to spin degeneracy, suggests an alternative to T centers as a high-fidelity spin-photon interface.

I. INTRODUCTION

Building a practical quantum network is essential to scale the computational power and application of quantum computers and to support the development of secure quantum communications^{1–4}. To send the flying qubits (photons) over long distances, the current fiber communication infrastructure is in the telecommunication wavelengths centered around 1310 nm (O-band) and 1550 (C-band), and an intermediate node such as a quantum repeater can further increase the communications and network range^{5–13}. For this purpose, high-dimensional energy-time entangled qubits can be an important platform to carry quantum information efficiently with high information capacity between high-fidelity quantum memory nodes^{14–17}. Moreover, for low error-rate communications, operating the high-dimensional quantum channels near the fiber zero-dispersion wavelength around 1310 nm is desirable, wherein the timing errors are minimal over long distances, increasing state fidelity. Thus, it is essential to develop a high-fidelity quantum node with near-unity radiative efficiency, devoid of possible non-radiative pathways and can be integrated with integrated photonic devices to interface with O-band quantum channels. The increased excited state lifetime of defect center due to the elimination of non-radiative pathways, can be improved by integration with cavity structures towards high-coherence fast photonic qubit interactions.

Solid-state color center qubits in silicon hosts are examined as prominent candidates for quantum nodes due to several reasons^{18–20}. Silicon is the dominant, scalable, and well-designed platform for the nanoelectronic and nanophotonic circuits to control and interface with our qubits. It is possible to create reproducible color centers and donor defects with exceptional characteristics. Furthermore, recently developed ^{28}Si substrates that are isotopically purified up to 99.9998% offer a host devoid of magnetic field fluctuations, supporting good qubit coherence^{21–25}. Remarkably, spin qubits with long lifetimes of up to 3 hours for shallow phosphorus donors²⁶, and 2.14 s for deep selenium donors^{27,28} have been developed. Phosphorus donors operate in the microwave regime, and se-

lenium donors have a mid-infrared transition, which is less expeditious to interface with the current fiber network infrastructure.

Color centers in silicon based on G, W, and T defects are a promising platform due to the available generation processes, with bright photoluminescence (PL) emissions near the O-band, long lifetimes, and narrow emission linewidths^{29–39}. Compatible with silicon photonic devices, G and W centers have been examined as bright single-photon sources with their singlet-singlet transitions. However, the G and W centers lack a spin-photon interface for information storage^{38–40}. T centers, on the other hand, are proposed as a suitable candidate due to the efficient, coherent spin-photon interface in the telecommunication wavelengths^{41–46}. It is shown to have a doublet-line (TX_0 and TX_1) with 1.76 meV spacing, most likely resulting from internal stress⁴⁷. The atomic composition of T centers is shown to be two carbon atoms occupying a single silicon site, while a hydrogen atom is bonded with one of the carbon atoms with C_{1h} symmetry⁴⁸. It is proposed that the T center is formed by capturing an interstitial carbon-hydrogen complex at a substitutional carbon site. Electronically, the T center site includes a bound exciton and an unpaired electron, where two electrons constitute a spin-0 singlet state, while the unpaired hole has a spin-3/2 state⁴⁷. The first (TX_0) and second (TX_1) excited state transitions of T centers are measured at ≈ 1325.9 nm (935.1 meV) and 1323.4 nm (936.86 meV) respectively⁴¹, close to the O-band zero-dispersion wavelength. The ensemble linewidth of TX_0 zero-phonon line (ZPL) for an ensemble of T centers is measured as 26.9 μeV in natural silicon and 0.14 μeV in ^{28}Si . The measured TX_0 lifetime is 0.94 μs , leading to a possible ZPL dipole moment of 0.73 Debye and a Debye-Waller factor of 0.23 at 1.4 K⁴¹. Spin resonance measurements have shown a nuclear spin coherence time over a second from Hahn echo. These properties make T centers an attractive platform for a metropolitan-scale quantum network.

In this work, we observe a unique 0.56 meV-split doublet at 1312.15 nm (943 meV) with a possible spin-photon interface, even closer to zero-dispersion wavelength, and along-

side the T center transitions. This photoluminescence line is attributed to a transition-metal defect comprising Cu and Ag atoms called $^*Cu_n^m$, with an isoelectronic bound exciton similar to T centers^{49–51}. The $^*Cu_n^m$ defect is first discovered by McGuigan et al. in a lightly Cu-doped silicon substrate alongside another defect around 1221 nm (1014 meV), termed Cu and comprises four Cu atoms^{50,52,53}. The possible ground triplet state of $^*Cu_n^m$, similar to NV-centers in diamonds, is seen as a good candidate for stable, high-fluence qubits^{33,34}.

We study the photophysics and cryogenic microphotoluminescence (μ PL) spectroscopy of the $^*Cu_n^m$ doublet transitions, comparing it with the T center doublet, including pump power dependences, temperature dependences, lifetime measurements with thermal partition function and rate analyses. Electron spin resonances and magnetic field measurements on the $^*Cu_n^m$ transitions are examined. We further describe the process steps to improve the T center and the $^*Cu_n^m$ generation to develop optical spin-photon interfaces towards quantum memories or repeaters. For this purpose, we examine and identify the relevant transformations between the plethora of color centers. We report an increased TX_0 lifetime up to 1.56 μ s, owing to process optimization leading to less lattice distortion, and examined its bound exciton dynamics using a rate equation model to assess the carrier feeding process from higher excited states. These color centers have the unique potential for interfacing with energy-time entangled photonic qubits toward high-rate quantum communications.

II. SAMPLE PREPARATION AND PROCESS VARIATIONS

We examine a combination of different ion implantation and rapid thermal annealing processes to control and optimize the color center defect generation processes. Here, the T centers are generated by the following process adapted from earlier studies^{54,55}. A float-zone (FZ) grown, dilute boron-doped silicon substrate, whose resistivity is 1000 to 2000 $\Omega \cdot cm$ with carbon and hydrogen impurity concentrations less than $2 \times 10^{16} cm^{-3}$, is used. First, carbon ions are implanted into the silicon substrate at 7 degrees with 38 keV energy and a dose of $7 \times 10^{12} cm^{-2}$. This implantation recipe produces an ion profile whose peak concentration is at 118.8 nm from the surface with 42.8 nm straggle based on SRIM-2013 simulations, with profile shown in Figure 1a-i⁵⁶.

The lattice damage from carbon implantation is repaired by rapid thermal annealing (RTA) at 1000 °C for 20 seconds in an argon environment with a flow rate of 3,000 sccm. The maximum temperature is achieved after a 28-second ramp-up, while the cooling is done passively under high argon flow (20,000 sccm). The temperature profile used is shown in Figure 1a-ii. This recipe is commonly used to introduce substitutional carbon centers in silicon to form G centers, which are examined as single-photon emitters^{30,31,40}. In order to promote C-H groups needed to form the T centers, we subsequently implant hydrogen ions into the silicon substrate at 7 degrees with 9 keV energy and a dose of $7 \times 10^{12} cm^{-2}$. As a result of this implantation, we obtain a hydrogen concen-

tration profile illustrated in Figure 1a-iii with a peak concentration at 120.8 nm from the surface and with a straggle of 38 nm, matching the carbon concentration⁵⁶. These samples are then cleaned using acetone and isopropyl alcohol and N_2 blow-dried.

Afterward, the samples are treated in deionized water to promote hydrogen diffusion and bonding with carbon atoms. The treatment is done in a cleanroom setting under a fume hood, using a hot plate with a two-step process. The samples are treated in deionized water with a hot plate temperature of 115 °C for 30 minutes, subsequently with the hot plate increased to 180 °C and held for 37 minutes (Figure 1a-iv). Two-step treatment under fume hood is optimized to apply a controllable amount of thermal energy, with water surface temperature up to 95.5 °C. The treated samples are placed into the RTA chamber as the last step to promote the binding of C-H groups with substitutional carbon sites to form T centers. Inside the nitrogen environment, the samples are annealed at 420 °C for 3 minutes within a SiC susceptor, whose thermal properties may affect the actual temperature. The duration of annealing is varied to examine the changes. We also tested the outcomes when the samples were annealed without H_2O treatment, which is important to protect the samples from oxygen contamination that contributes to the broadening of T center emissions.

Figure 1b shows the μ PL spectrum taken between 1100 and 1400 nm at 5 K after each process step to examine the T center formation mechanism and its precursors compared to untreated Si substrate. As a benchmark of lattice damage in silicon, it can be observed that the silicon transverse-optical (TO) transition line around 1130 nm (bandgap) is completely destroyed under carbon implantation, which is recovered by RTA in step ii⁵⁷. Owing to the low atomic mass, hydrogen implantation only shows a 10% decrease in Si TO line compared to step ii. Interestingly, the subsequent deionized water treatment also acts as an annealing process, which enhances the Si TO line damaged by hydrogen implantation. After the second RTA step, we observe a 30% decrease in Si TO line intensity, which might be due to the replacement of the Si sites with C-(C-H) complex that leads to the T centers formation⁴⁷. We observe a similar trend in the Si phonon replica around 1195 nm. Superimposed on the phonon replica, after step v, we observe the presence of the weak X center line at 1191.7 nm. The origins of the X center are uncertain; initial propositions pointed out an interstitial nature with a possible tetrahedral or tetragonal symmetry, while the recent ab-initio studies on candidates such as I3-X or I4-A defects are inconclusive⁵⁸.

After carbon implantation at step i, prior to rapid annealing of the resulting lattice damage, we clearly observe the formation of W and G centers whose ZPL transitions are at 1217.48 nm and 1278.5 nm, respectively, with Gaussian full-width-at-half-maximum (FWHM) linewidths around 0.65 nm and 0.8 nm. The G center is a carbon-related defect, thought to be composed of two substitutional carbon sites connected by interstitial silicon^{30,31}. Here we observe the G line clearly without any annealing. The lifetime of the produced G center is also measured up to 6.67 ns at 7.5 K, which is slightly longer than the 5.9 ns reported previously for the ensembles but in-

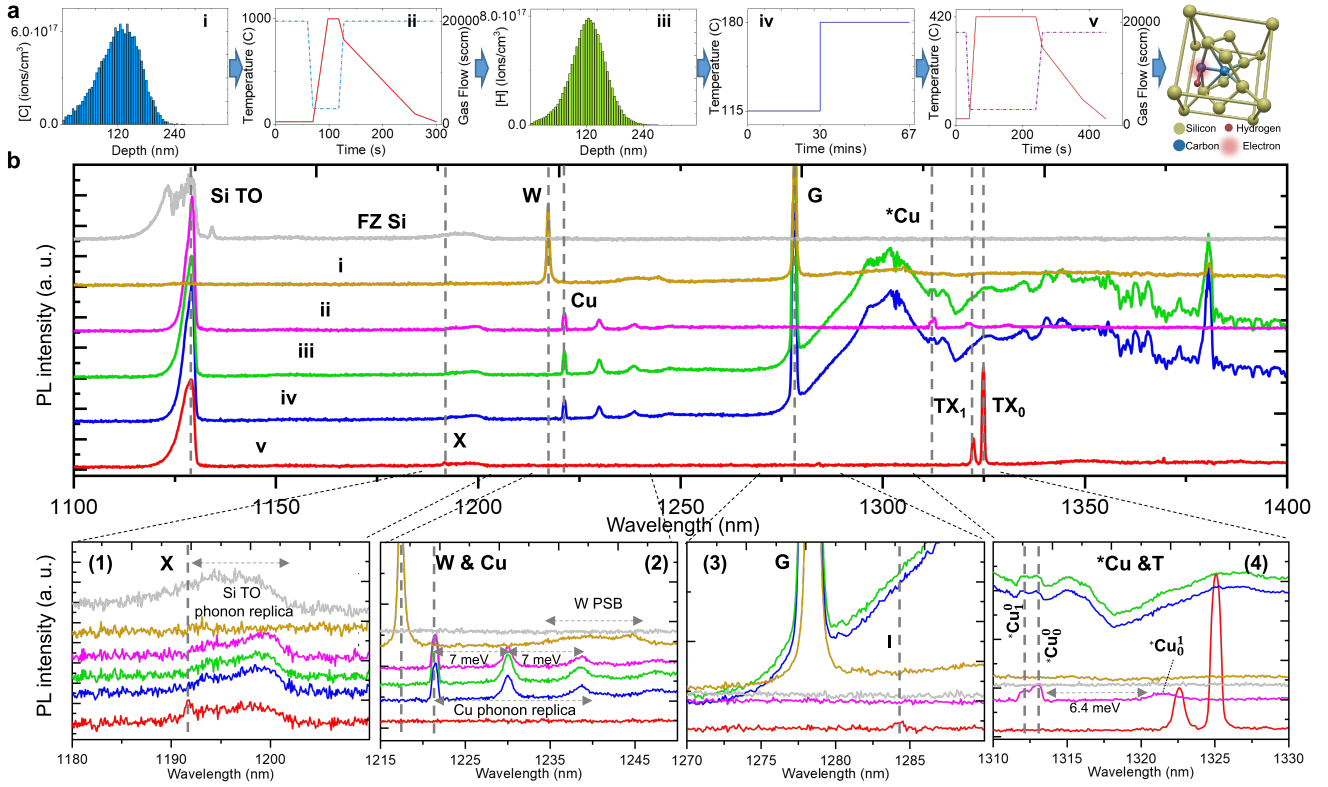


FIG. 1. Family of color centers in silicon and the T center generation recipe — **a**, Process steps: i) Simulated depth profile of carbon implantation with 38 keV ion energy. ii) Temperature (solid line) and gas flow (dashed line) profiles for rapid thermal annealing recipe at 1000°C for 20 seconds. iii) Simulated depth profile of hydrogen implantation with 9 keV ion energy. iv) Hot plate temperature variation for H₂O treatment. v) Temperature (solid line) and gas flow (dashed line) profiles for rapid thermal annealing at 420°C for 3 minutes. **b**, Change in the μ PL spectrum at each process step, where each identified line is marked with dashed lines and the spectra are stacked with equal spacing vertically for easier identification. The X, W, G, and T emission lines are magnified at the bottom. The observed 0.56 meV-split $^*\text{Cu}$ doublet around 1312.15 nm is denoted as the low ($^*\text{Cu}_0^0$) and high ($^*\text{Cu}_1^0$) energy line.

indicates the dominance of nonradiative processes^{30,35}. The W line has a phonon sideband up to 1250 nm, while the G line phonon sideband extends up to 1400 nm, including a local vibrational mode at 1381 nm⁵⁹. Annealing at 1000 °C for 20 seconds, as shown in 1a-ii, however, leads to the disappearance of the G and W lines. This disappearance indicates the displacement of implantation-induced silicon interstitials into the lattice during thermal annealing. The W line is thought to be a cluster of interstitial silicon atoms in the lattice with a ZPL around 1218 nm^{58,60–62}.

The W line is replaced in step ii by three phonon replicas at 1221.45, 1230.07, and 1238.64 nm with FWHM of 0.58, 1.2, and 1.65 nm, respectively, as shown in Figure 1b. These lines are about 7 meV apart from each other, indicating the energy of the involved phonons. The peak energies and separation are aligned with prior literature where it is identified as the Cu line, a complex of four Cu atoms^{50,52,63,64}. We observe a similar structure for the $^*\text{Cu}_n^m$ doublet peak around 1312.15 nm (Figure 1b-4 and Figure 2a), consisting of 0.56 meV split low ($^*\text{Cu}_0^0$) and high ($^*\text{Cu}_1^0$) energy lines at 1312.98 and 1312.20 nm respectively. Here, the superscript, m, indicates the number of phonons involved in the transition, hence

denoting the phonon replicas, while the subscript, n, indicates the order of the transition in the excitonic energy ladder. We also observe alongside 6.4-meV phonon replicas at 1321.64 nm (called $^*\text{Cu}_1^0$) and 1331.06 nm (called $^*\text{Cu}_2^0$). These spectral peaks are formed after carbon implantation and RTA at 1000 °C, after step ii. We explain the fortuitous formation of Cu and $^*\text{Cu}_n^m$ peaks by possible Cu contamination during implantation and annealing steps, whose SIMS depth profile is given in Supplementary Materials as evidence. The Gaussian FWHM linewidth of the $^*\text{Cu}_0^1$ peak is around 0.66 nm, while the $^*\text{Cu}_0^0$ peak has a linewidth of 0.523 nm. These peaks disappear when deionized water treatment is applied. When we applied step v RTA process, without any water treatment, we were able to observe $^*\text{Cu}_0^0$ and $^*\text{Cu}_1^0$ peaks alongside the T center TX₀ and TX₁ lines, while the phonon replica at 1321.64 nm shows itself as a shoulder peak to TX₁, denoted by $^*\text{Cu}_1^0$.

The RTA-only treatment is shown as the blue line dataset in Figure 2a. Our initial studies using secondary-ion mass spectroscopy verify the earlier studies that both the lines at 1221.45, 1230.07, and 1238.64 nm and the doublet denoted as $^*\text{Cu}_0^0$ and $^*\text{Cu}_1^0$ originate from residual Cu and/or Ag constituents during implantation. The 1221.45 nm line and the 7

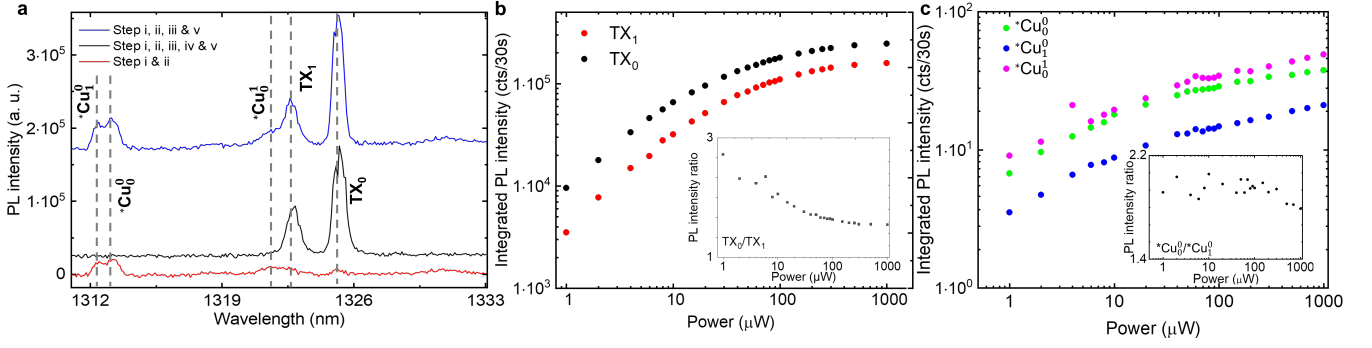


FIG. 2. **Cryogenic microphotoluminescence character of TX₀, TX₁ and $^{*}\text{Cu}_n^m$ transitions in silicon.** — a) PL spectrum showing the formation of TX₀, TX₁, $^{*}\text{Cu}_0^0$, $^{*}\text{Cu}_0^1$, and $^{*}\text{Cu}_1^0$ peaks at different process steps b) Pump power dependence of the TX₀ and TX₁ PL integrated areas. Inset: ratio of TX₀/TX₁ intensities with increasing pump power. c) Pump power dependence of the $^{*}\text{Cu}_0^0$, $^{*}\text{Cu}_0^1$ and $^{*}\text{Cu}_1^0$ PL integrated areas. Inset: ratio of $^{*}\text{Cu}_0^0$ / $^{*}\text{Cu}_0^1$ intensity with increasing pump power.

meV-apart phonon replicas are identified as Cu-line, which is a precipitation of four Cu atoms^{49,50,64,65}. On the other hand, the 1312.15 nm doublet line and its phonon replica with 6.4 meV phonon energy at 1321.64 nm, belongs to a defect where a single Ag atom displaces one of the Cu atoms in the Cu-line, which is denoted as the $^{*}\text{Cu}$ center^{49–53,66}. We were able to replicate the formation of Cu and $^{*}\text{Cu}_n^m$ lines with deliberate Cu and Ag implantation into a Si wafer and RTA at 900 °C for 20 seconds, whose PL spectrum is provided in Supplementary Materials. We should also note that, as shown in Figure 2a, both the T centers and $^{*}\text{Cu}$ centers can be present simultaneously when water treatment is omitted, which suggests that $^{*}\text{Cu}$ center is also susceptible to hydrogenation under available thermal budget, either via implantation or deionized water treatment used for hydrogen diffusion.

The G center emission is recovered after hydrogen implantation. It results from the implanted-proton-induced interstitials and persists after the deionized H₂O treatment⁶⁷. However, it has a high-intensity phonon sideband from 1280 nm to 1400 nm, with the previously reported E-line evident at 1381 nm^{59,68}, as observed in step i. Furthermore, after step v, a small peak is observed around 1285 nm, corresponding to the I-center, a variation of the T center perturbed by the presence of oxygen atoms⁶⁹. The oxygen concentration $[\text{O}]$ is less than $2 \times 10^{16} \text{ cm}^{-3}$ in the substrate.

As a result of the two-step H₂O treatment and RTA at 420 °C for 3 minutes, we obtained a clean TX₀ zero-phonon line at 1325.1 nm with 0.63 nm linewidth and a TX₁ line at 1322.65 nm with 0.79 nm linewidth. Figure 2a shows the TX₀ and TX₁ lines in the samples that are carbon and hydrogen implanted (after step iii), H₂O and RTA treated (after step v), and also the case where the samples are RTA treated only after step iii (without H₂O treatment). This indicates that, although deionized H₂O treatment facilitates high-purity sample development, it is not required to induce T-center formation⁵⁵.

The integrated intensity of TX₀ and TX₁ emissions as a function of pump power is given in Figure 2b. The ZPL intensity area is saturated around 300 μW. Presented in Figure 2b inset, at 1 μW pump power, the ratio of ZPL intensity between TX₀ and TX₁ is around 2.725, which gradually decreases and

reaches a minimum plateau point around 300 μW where TX₀ states saturate, while the optically injected carriers keep populating the TX₁ states up to 500 μW.

The same analysis is done for $^{*}\text{Cu}_0^0$ and $^{*}\text{Cu}_0^1$ peaks and the shoulder ($^{*}\text{Cu}_1^0$) peak we have discussed before. Similar to TX₀ and TX₁, the $^{*}\text{Cu}_0^0$ and $^{*}\text{Cu}_0^1$ intensities exhibit a saturation behavior at high pump power. Note that the broad $^{*}\text{Cu}_1^0$ line at the lower energy side of $^{*}\text{Cu}_0^0$ and $^{*}\text{Cu}_0^1$ lines follows the same trend as $^{*}\text{Cu}_0^0$ and $^{*}\text{Cu}_0^1$, suggesting it can be attributed to a phonon replica. Unlike the T center, the intensity ratio between $^{*}\text{Cu}_0^0$ and $^{*}\text{Cu}_0^1$ begins around 2, staying constant up to 100 μW, and slowly decreases at higher power. Note that Cu center phonon replicas appear at the higher energy side of $^{*}\text{Cu}_0^0$ and $^{*}\text{Cu}_0^1$ lines (between 1221 nm and 1240 nm) (Figure 1b-2) while the T center spectrum (Figure 1b-4) is clean. As a result, a delayed decrease of the $^{*}\text{Cu}_0^0$ and $^{*}\text{Cu}_0^1$ intensity ratio can be due to the efficient carrier captured by the Cu centers.

A. Temperature dependent micro photoluminescence spectroscopy on T-center and $^{*}\text{Cu}$ defects

To investigate the nature of the observed $^{*}\text{Cu}$ doublet emission at 1312.15 nm, we performed a comparative study of the temperature-dependent μPL spectroscopy on the T center ZPL. Under low injection below μPL intensity saturation, Figure 3a shows the temperature-dependent μPL spectra of the $^{*}\text{Cu}_1^0$, $^{*}\text{Cu}_0^0$ and $^{*}\text{Cu}_0^1$ lines from 4.5 K to 30 K on an FZ silicon sample with carbon implantation and subsequent RTA process detailed in step i and ii of Figure 1a. A similar temperature-controlled measurement on the T center ZPL (TX₀ and TX₁) from 4.5 to 40 K is also performed on an FZ silicon sample with the fabrication process up to step v, and the μPL spectra are shown in the Supplementary Materials. Both defects show an isotropic dependency on the excitation polarization of the excitation as expected from an ensemble of doublets. In Figures 3b and 3c, it is shown that there is no preference of polarization between the doublets TX₀-TX₁ and $^{*}\text{Cu}_0^0$ - $^{*}\text{Cu}_0^1$, which may cause a population transfer between them.

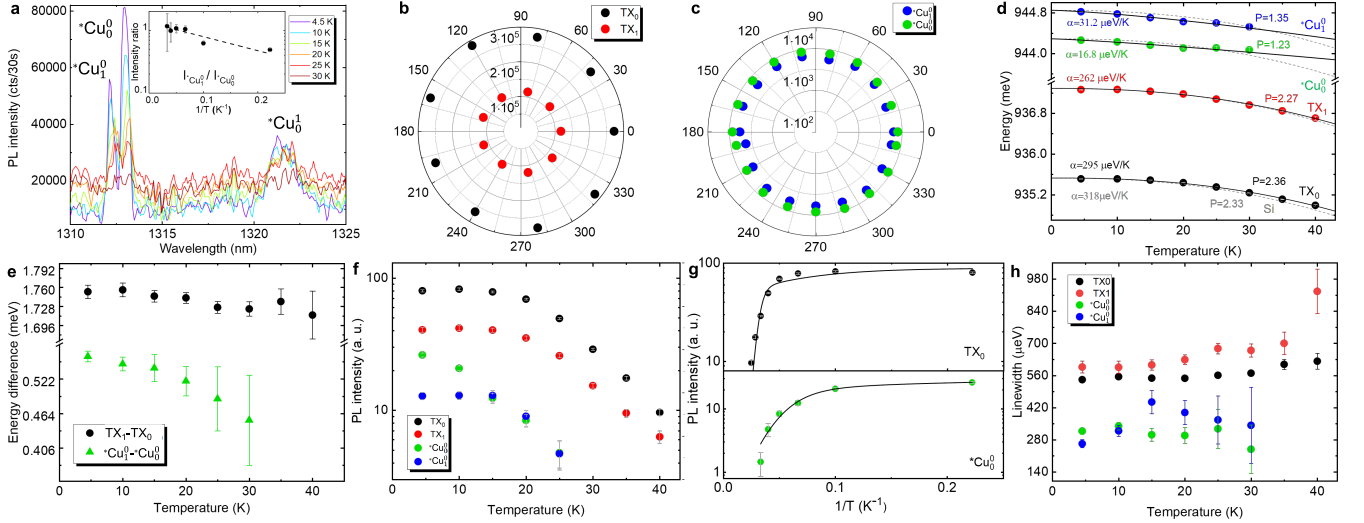


FIG. 3. **Temperature and polarization dependence of micro photoluminescence on T-center ZPL (TX₀ and TX₁) and *Cu doublet at 1.313 μm (*Cu₀⁰ and *Cu₀¹)** — **a.** Temperature-dependent μ PL spectra of *Cu₁⁰, *Cu₀⁰ and *Cu₀¹ lines. Inset: Intensity ratio of *Cu₁⁰/*Cu₀⁰ as a function of reciprocal temperature. **b.** Polarization-dependent PL of T center ZPL (TX₀ and TX₁) and **c.** *Cu₀⁰ and *Cu₀¹ emissions show an isotropic behavior as expected from the ensemble properties. **d.** ZPL transition energy of TX₀ (black dot), TX₁ (red dot), *Cu₀⁰ (green dot), and *Cu₀¹ (blue dot) as a function of temperature. The red solid and dashed curves denote the fit by the four-parameter Passler model⁷⁰. The grey dash curve is for bulk Silicon. **e.** The energy difference between *Cu₀⁰ and *Cu₀¹ and TX₀, TX₁ as a function of temperature. **f.** TX₀ (black dot), TX₁ (red dot), *Cu₀⁰ (green dot), and *Cu₀¹ (blue dot) integrated ZPL intensity as a function of temperature. **g.** The intensity of TX₀ and *Cu₀⁰ as a function of reciprocal temperature. The solid red curves denote the fits by Eq. (3). **h.** TX₀ (black dot), TX₁ (red dot), *Cu₀⁰ (green dot), and *Cu₀¹ (blue dot) linewidth as a function of temperature.

Figure 3d presents the temperature dependences of the *Cu₀⁰, *Cu₀¹, and T-center ZPL transition energies extracted from Gaussian fits of their spectra. At cryogenic temperatures, the thermal-induced redshift of the semiconductor bandgap can be well expressed by the four-parameter model,

$$E(T) = E(0) - \alpha\Theta/2p (2T/\Theta)^p \quad (1)$$

where α denotes the slope dE/dT in the limiting case of $T \rightarrow \infty$, p is a dimensionless parameter related to the phonon dispersion coefficient $\sqrt{\frac{\langle \epsilon_{ph}^2 \rangle - \langle \epsilon_{ph} \rangle^2}{\langle \epsilon_{ph} \rangle}}$, and Θ approximately equals to the average phonon temperature⁷⁰. For simple fitting purposes, Eq. (1) can be rewritten as a polynomial expression,

$$E(T) = E(0) - AT^p. \quad (2)$$

The transition energy of *Cu₀⁰, *Cu₀¹, and T-centers are fitted using Eq. (2) and represented by the red curves. The dimensionless fitting parameter p is equal to 1.25, 1.23, 2.27, and 2.36 for *Cu₀⁰, *Cu₀⁰, TX₁, and TX₀ transitions respectively. For comparison purposes, since the defect centers are in a sea of silicon atoms, we assume the average phonon temperature is the same and equals $\Theta \approx 406K$ for silicon⁷⁰. We can then extract the value of α to be 31.2, 16.8, 262, and 295 $\mu\text{eV/K}$ for *Cu₀⁰, *Cu₀⁰, TX₁, and TX₀ respectively. The silicon band gap variation with temperature is also plotted as grey dash lines along with the *Cu₀¹, *Cu₀⁰, and T center by setting the parameters for silicon to be $p = 2.33$, $\alpha = 318\mu\text{eV/K}$,

and $\Theta \approx 406K$ from⁷⁰. For TX₀ and TX₁, their parameters are close to silicon values which indicates a smaller modification of the silicon matrix by the T center in the sample where steps i to v are performed. It suggests that the annealing and H₂O treatment, which promotes the migration of carbon and hydrogen interstitials and leads to the T center formation, restore the lattice efficiently. In stark contrast, the red-shifting behavior of *Cu₀⁰ and *Cu₀¹ transition energy exhibits a dramatic deviation from the silicon bandgap, resulting in a much smaller fitting parameter of p and α compared with the silicon and T center. This suggests that a significant distortion of the silicon matrix occurs during step i, where the injected carbon ions and displaced silicon atoms occupy the interstitial sites, creating vacancies in the implantation path.

The step ii promotes the impurity migration and results in the formation of 0.57 meV-split doublet luminescence centers. Notably, a much lower value of p and α result in a more significant phonon dispersion, and a smaller slope at $T \rightarrow \infty$ suggests smaller zero-point renormalizations⁷¹ by the dramatic modification of the electron-phonon interaction during its formation processes. This can also be in line with the observation of the vanishing W center ZPL and the appearance of phonon replicas. The significant phonon dispersion also leads to a higher dependence of doublet splitting of the *Cu₀⁰ and *Cu₀¹ lines compared to the T center doublet. In Figure 3e, we observe that the energy difference between the *Cu₀⁰ and *Cu₀⁰ lines is reduced by at least 0.1 meV till about 30 K, before thermalization. On the other hand, the energy difference between TX₀ and TX₁ are somewhat constant across temper-

atures, owing to the smaller modification of the silicon matrix.

Figure 3f shows the integrated intensities of the $^*\text{Cu}_0^0$, $^*\text{Cu}_0^1$ lines, and T centers ZPL with increasing temperatures. TX_0 and TX_1 start to thermalize around 20 K, while the $^*\text{Cu}_0^0$ line quenches much earlier. The intensity of the $^*\text{Cu}_0^1$ line exhibits a plateau up to 15 K. The measured 1.75 ± 0.0113 meV spectroscopic splitting between the TX_0 and TX_1 lines at 4.5 K matches the reported value⁷². The known dissociation energy of the bound exciton of 22.5 meV⁷² can be well-reproduced by fitting the TX_0 intensity (black dots in Figure 3c) by a thermal partition function,

$$I(T) = \frac{I(0)}{1 + A \exp(-\frac{E_1}{kT}) + BT^{3/2} \exp(-\frac{E_2}{kT})} \quad (3)$$

and setting $E_1 = 1.75$ meV as the excess energy of the excited state TX_1 to TX_0 and $E_2 = 22.5$ meV as the activation energy to the silicon band edge, which is shown as the black curve in the upper panel of Figure 3g. For the $^*\text{Cu}_0^0$ and $^*\text{Cu}_0^1$ lines, it is worth noting that their integrated intensity ratio $\frac{I_H}{I_L}$ (inset of Figure 3a) leads to a Boltzmann factor with a thermal activation energy of $E_a = 0.44 \pm 0.12$ meV which agrees with the measured spectroscopic splitting of 0.56 ± 0.0089 meV within our experimental error. It suggests that, like TX_1 and TX_0 , the $^*\text{Cu}_0^1$ line can be associated with a transition from the higher excited state to the lower $^*\text{Cu}_0^0$ state of the same defect center. As shown in the lower panel of Figure 3g, Eq. (3) can be used to fit the $^*\text{Cu}_0^0$ intensity by setting E_1 to be the measured spectroscopic doublet splitting of 0.56 meV, with the resulting $E_2 = 3.35$ meV when the fit converges. This suggests a much smaller binding energy than the T center bound excitons and agrees with the much earlier intensity quenching of $^*\text{Cu}_0^0$ line even below 10 K. The total binding energy E_B of the electron and hole associated with the bound exciton localized to this defect color center can be deduced to be 225.2 meV by subtracting transition energy of $^*\text{Cu}_0^0$ by the silicon bandgap at low temperature. Like the T center, $E_B \gg E_2$ probably suggests that such 0.57 meV-split doublet related luminescence center consists of one strongly localized and another loosely Coulombic bound particles, which is potentially another candidate for a spin-photon interface in the telecommunication band. Note that the μPL intensity plateau of the $^*\text{Cu}_0^1$ line below 15 K is likely due to the thermal-induced carrier populating from the lower energy $^*\text{Cu}_0^0$ state to $^*\text{Cu}_0^1$.

Figure 3h shows the temperature variation of FWHM linewidth. Both the lower energy states, TX_0 and $^*\text{Cu}_0^0$ of the T-center and 0.56 meV-split doublet, exhibit a constant linewidth of about 542 μeV and 318 μeV , respectively, within our experimental error. However, for the higher energy states, TX_1 linewidth stays constant at about 598 μeV till around 20 K and increases to 927 μeV at 40 K. The $^*\text{Cu}_0^1$ linewidth increases from 263 μeV to 444 μeV from 4.5 K to 15 K. It then gradually decreases to 343 μeV at 30 K. The observed broadening with respect to the Fourier transform-limited linewidth of T center (≤ 1 neV) can result from: (1) fluctuating environmental charges which lead to pure exciton dephasing, or spectral diffusion, depending on the rate of energy Stark shifting; (2) ensemble emitting centers where individual ZPLs are

shifted due to different local strains; (3) isotopic effects from natural silicon, in which the ^{29}Si with non-zero nuclear spin cause resonance shift and magnetic field fluctuations; and (4) phonon-assisted broadening. However, for temperature variation of the linewidth, the phonon contribution is not significant for $T = 30$ K. We thus attribute the broadening of TX_1 with temperature ≤ 30 K due to increasing charge fluctuations as a result of the thermal-induced electrons with increasing temperatures, considering the low pump regime (32 μW). The sudden increase at high temperature (40 K) can be due to increased phonon population and scattering. The minor variation of the TX_0 linewidth compared to the TX_1 linewidth can be due to its more localized exciton wavefunction, which also applies to the constant behavior of linewidth for the lower energy $^*\text{Cu}_0^0$ state compared to the higher energy doublet state. The dramatic increases of $^*\text{Cu}_0^1$ linewidth up to 30 K, in line with its thermalization above 30 K as shown in Figure 3f, can be attributed to increased charge fluctuations from the thermally-induced carriers, considering the small activation energy of 0.56 meV from $^*\text{Cu}_0^0$ to $^*\text{Cu}_0^1$ state. The subsequent decrease in the $^*\text{Cu}_0^1$ linewidth can be due to the charge stabilization of the fully occupied $^*\text{Cu}_0^1$ states at higher temperatures.

B. Photoluminescence dynamics of T-center and $^*\text{Cu}$ defects

The lifetime of the T center, a most likely candidate for next-generation spin-photon interface, was previously reported²⁸ but its radiative and non-radiative bound exciton dynamics are rarely studied. Thus, we performed the temperature-dependent time-resolved photoluminescence (TRPL) measurements on TX_0 and TX_1 color center transitions. We excite the sample with a pulse laser (600 nm, pulse width ≈ 5 ps) from an angle of about 45 degrees with the sample surface via a plano-convex singlet lens, creating a large excitation spot diameter of about 40 μm . We achieved sufficient counts for the TRPL histogram integration while refraining from saturating the T centers. μPL is collected from the excitation spot via a $20\times$ ($\text{NA} = 0.4$) microscope objective perpendicular to the sample surface and passes through a 0.5-meter monochromator to a near-infrared (NIR) photomultiplier tube (PMT) unit with ≈ 400 ps timing resolution attached to the exit port. The TRPL is then performed with the time-correlated single-photon counting (TCSPC) technique. The high-density 1200 grooves/mm grating achieves a spectral resolution of 0.04 nm so that only the ZPL of TX_0 or TX_1 feeds into the PMT, and the phonon sideband photons are rejected.

Figure 4a shows the resulting TRPL traces of TX_0 transition with sample temperatures varying from 5 K to 40 K. The TX_0 μPL decay exhibits a prolonged tail and remains unchanged with increasing temperature until reaching 20 K, where it changes to a fast decay. Interestingly, as shown in the inset of Figure 4a, a slow rise of the TX_0 PL intensity is visible at 5 and 10 K and gradually vanishes with increasing temperature. Such a slow rise component of the μPL inten-

sity and its variation with temperatures are neither observed in TX₁ states and G centers (see Supplementary Materials), and nor observed in prior W⁶⁰, G^{30,31} and T centers^{28,54,55}. We speculate that the carrier transition to TX₀ from the higher excited states (TX₂ to TX₂₅) leads to a slow rise with the peak photoluminescence²⁸. We phenomenologically explain this process using a simple two-level system coupled to the continuum of states, as shown in the inset of Figure 4b.

The measured μ PL decay of TX₀ can be interpreted as the carrier relaxation from TX₀ to a ground state with a lifetime τ_0 (radiative and non-radiative) and a non-radiative carrier feeding from an effective higher excited state $n_{ex}(t)$ to TX₀ with a characteristic time constant τ_f . Note that since the carrier transition from the silicon band edge is fast (tens of fs)^{73,74} it cannot be resolved in the measurement and thus absorbed into the initial carrier populations $n_0(0)$ and $n_{ex}(0)$. The following rate equations describe the carrier populations of $n_0(t)$ and $n_{ex}(t)$:

$$\frac{dn_0}{dt} = -\frac{n_0}{\tau_0} + \frac{n_{ex}}{\tau_f} \left(\frac{N_0 - n_0}{N_0} \right) \quad (4)$$

$$\frac{dn_{ex}}{dt} = -\frac{n_{ex}}{\tau_{ex}} - \frac{n_{ex}}{\tau_f} \left(\frac{N_0 - n_0}{N_0} \right) \quad (5)$$

where n_0 and n_{ex} are the populations of the optically excited carriers in TX₀ and higher excited states respectively. τ_0 is the decay time of the TX₀ state, and τ_{ex} is the effective lifetime of higher excitation states. τ_f denotes the characteristic time constant of the non-radiative carrier feeding to TX₀ states. N_0 denotes the total amount of available TX₀ states that can be occupied.

As shown in Figure 4a, the TRPL trace of TX₀ can be well-fitted by the model, and the extracted fitting parameters are shown in Figure 4b as a function of temperature. We extract a prolonged decay time of $\tau_0 = 1.56 \pm 0.13 \mu s$ at 5 K, which is 65% longer than the previously reported 0.94 μs decay time²⁸, and is much closer to expected lifetimes between 2 to 10 μs ⁷⁵. With increasing temperatures, τ_0 decreases to 26 ± 0.24 ns at 40 K, where TX₀ emission almost vanishes. Importantly, we observe the carrier transition lifetime of $\tau_f = 11 \pm 0.3$ ns at 5 and 10 K, which contributes to the clear slow rising of TRPL traces and suddenly becomes slower with $\tau_f = 50 \pm 0.3$ ns at 30 K. The observed 11 ns carrier transition and the resulting slow μ PL rising only observed for TX₀ below 10 K can be caused by a much more localized nature of TX₀ states. τ_f is three orders of magnitude faster than the decay of TX₀, indicating a strong coupling between the localized TX₀ and delocalized higher excited states.

Considering that the pump power is fixed for TRPL measurement at all temperatures, the ratio of initial occupation of TX₀ states to its total amount of available states, $\frac{n_0(0)}{N_0}$, show a sudden increase at 30 K, which indicates the start of thermal dissociation of TX₀ bound exciton. Note that, due to the much slower temporary features of the μ PL, the timing resolution of the detector (≈ 400 ps) is negligible in the fit. We also perform the rate equation fitting by setting $n_{ex} = n_1$, where n_1 denotes the TX₁ carrier population, but the simultaneous fitting of TX₁ and TX₀ μ PL decay cannot be achieved. It agrees

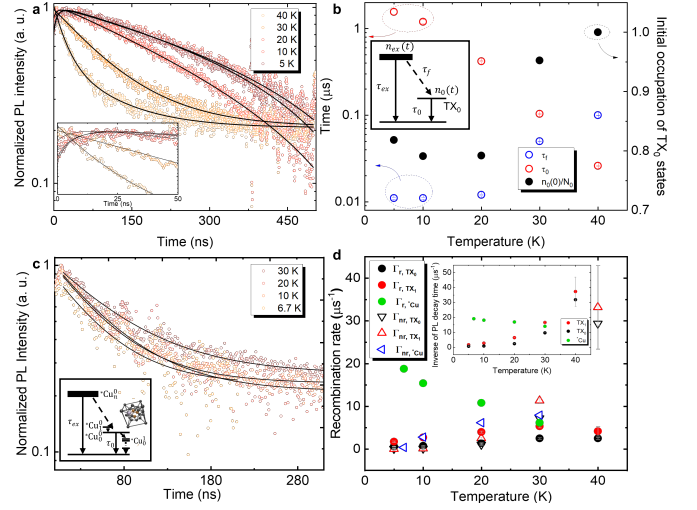


FIG. 4. T-center and $^*Cu_n^m$ bound exciton radiative dynamics. a. TRPL trace of TX₀ as a function of temperature-fitted rate equation. Inset: zoom-in of early TRPL rise time. **b.** Radiative lifetime and carrier populations as a function of temperature, with the TX₀ state recombination mechanism depicted in the inset. The carrier populations of TX₀ and higher excited states are denoted as $n_0(t)$, and $n_{ex}(t)$ with corresponding lifetimes of τ_0 and τ_{ex} . τ_f denotes the relaxation time constant from the higher excited state to TX₀, and N_0 denotes the maximum available TX₀ states. **c.** TRPL trace of the combined doublet decay of $^*Cu_n^m$ exciton. **d.** The inverse PL decay time of TX₀, TX₁, and $^*Cu_n^m$ as a function of temperature. Inset: Bound exciton recombination rate as a function of temperature. Γ_{nr,TX_0} , Γ_{nr,TX_1} , Γ_{r,TX_0} , Γ_{r,TX_1} denote the nonradiative and radiative recombination rate of TX₀, TX₁, and $^*Cu_n^m$ accordingly.

with the hypothesis that the non-radiative carrier transition is dominated by higher excited states, which also corresponds to our case of the above silicon bandgap pumping. The coupling between TX₁ and TX₀ states can be a much faster process that can only be investigated by resonantly pumping the TX₁ state. Figure 4c shows the temperature-dependent TRPL of $^*Cu_0^0$ - $^*Cu_0^1$ lines. Due to the small 0.56 meV-splitting and experimental limitations, both $^*Cu_0^0$ and $^*Cu_0^1$ lines are measured together with a TRPL window between 1309 and 1316 nm. With the presence of higher disturbance in the lattice (larger deviation of dashed model lines from the temperature-dependent fit of measured $^*Cu_n^m$ data from Si lattice) in Figure 3d), the $^*Cu_0^0$ - $^*Cu_0^1$ decay occurs at a faster rate, with an excited state lifetime τ_0 of 52.4 ± 4.8 ns at 6.7 K. We observe an increase in the fitted lifetime at higher temperatures, to 71.2 ± 2.1 ns at 30 K, due to the population transfer from $^*Cu_0^0$ to $^*Cu_0^1$ and higher excited states with slower decay rates. To further investigate the T center bound exciton recombination dynamics, we assume that both the radiative Γ_r and non-radiative Γ_{nr} recombination channels contribute to the μ PL decay rate. The time-integrated μ PL intensity I of TX₀ and TX₁ at temperature T is proportional to the quantum efficiency $I(T) \propto \frac{\Gamma_r}{\Gamma_r + \Gamma_{nr}}$. With the radiative decay dominating the bound exciton recombination channel at T = 0 K, then I can be writ-

ten as:

$$I(T) = I(0) \frac{\Gamma_r}{\Gamma_r + \Gamma_{nr}} = I(0) \frac{\Gamma_r}{\Gamma_{tot}} \quad (6)$$

where $I(0)$ is extrapolated from Figure 3f and Γ_{tot} is the decay probability extracted from the rate equation fit of TX_0 or the single exponential fit of TX_1 . Then, the radiative recombination rate can be obtained from equation (6). The resulting μ PL dynamical parameters of TX_0 and TX_1 as a function of temperature are plotted in Figure 4d. The inverse of the μ PL decay time of TX_1 ($\tau_1 = 0.60 \pm 0.063 \mu s$) is nearly twice of TX_0 at 5 K and shows a sudden increase after 30 K in-line with TX_0 behavior. The extracted radiative and non-radiative bound exciton recombination rates of TX_0 and TX_1 , with the experimental error bars, are shown as the inset. Compared with the non-radiative rate, the radiative rate of both TX_0 (black circle) and TX_1 (red circle) is relatively constant $\approx 1.5 \mu s^{-1}$ and $3.6 \mu s^{-1}$ respectively, corresponding to a Fourier-transform limited linewidth of ≈ 0.494 neV and 1.19 neV. The relatively temperature-independent rates (below 30 K) indicate potentially the suppression of thermally-induced fluctuation of the bound exciton wavefunction along any direction due to the three-dimensional quantum confinement⁷⁶. A higher excited state (TX_1) is anticipated to be more delocalized, indicated by a larger TX_1 radiative rate. The slight increase in both TX_0 and TX_1 radiative rates with increasing temperature is due to the thermal-induced delocalization of the bound exciton wavefunctions. Above 30 K, the fast non-radiative decay starts to dominate both TX_0 and TX_1 recombination channels, which can be due to the thermal disassociation of bound excitons or the Shockley-Read-Hall (SRH) process induced by unwanted impurities or vacancies in natural Si, which results in the quenching of the T center μ PL intensity above 30 K. On the other hand, the radiative decay of combined $^*Cu_n^m$ emissions show an anomalous behavior, reducing with increased temperature from $18.76 \mu s^{-1}$ at 6.7 K to $6.13 \mu s^{-1}$ at 30 K, while the non-radiative recombination rate increase to $7.88 \mu s^{-1}$ and becomes the dominant decay channel. This counterintuitive phenomenon here is attributed to the difference in decay rates and multiple phonon-assisted decay pathways (phonon replicas). We speculate that $^*Cu_0^0$ decay is faster than $^*Cu_0^1$, which becomes dominant due to the population transfer at higher temperatures, as shown by the plateau in the $^*Cu_0^1$ observed in Figure 3f. After 30 K, the radiative decay of both $^*Cu_0^0$ and $^*Cu_0^1$ is thermalized by non-radiative and phonon-assisted decay through $^*Cu_1^q$ states, which is outside the spectral window of TRPL.

C. Magnetic-field induced broadening in the ensemble of and $^*Cu_n^m$ color centers

The T center bound exciton pairs with its ground state electron, which has a spin with an isotropic g -factor of $g_E = 2.0005$, to form a singlet with an unpaired hole spin with an anisotropic g -factor in TX_0 state⁵⁵. Under a magnetic field, the unpaired hole spin leads to Zeeman splitting and

diamagnetic shifts. The anisotropic hole spin leads to different g -factors and diamagnetic shift coefficients based on the orientation of the defect in the lattice⁴¹. The total shift in the peak energy for spin-dependent lines can be identified as $\Delta E = (\pm g_e \pm g_h) \mu_B B_z + \chi |B_z|^2$, where g_e and g_h are the g -factors for electron and holes, μ_B is the Bohr magneton, χ is the diamagnetic shift due to higher-order Zeeman effect, and B_z is the applied magnetic field⁷⁷. The splitting enables a spin-photon interface that is essential for quantum memory applications. For this purpose, we examined the 0.56 meV-split *Cu doublet luminescence centers under a magnetic field to assess their potential.

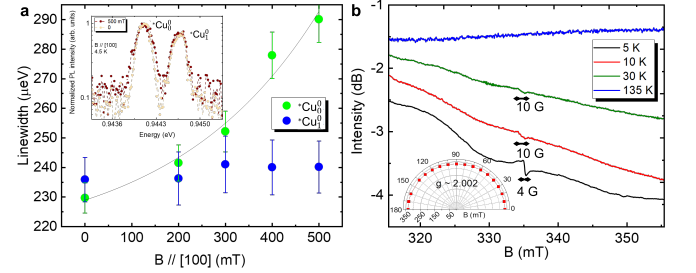


FIG. 5. Magnetic-field induced broadening in the ensemble of 0.56 meV-split doublet luminescence centers. **a.** The Voigt-profile linewidth of $^*Cu_0^0$ and $^*Cu_0^1$ lines under DC magnetic field with intensity up to 500 mT. Compared to the zero-field linewidth of 230 μeV , we observe an increase in inhomogeneous linewidth of the $^*Cu_0^0$ -line by 25% at 500 mT, while there is not a significant broadening in the $^*Cu_0^1$ -line. Inset: PL spectrum of $^*Cu_0^0$ and $^*Cu_0^1$ lines against DC magnetic field between 0 to 500 mT. The linewidth of the $^*Cu_0^0$ -line is fitted using a hyperbolic equation to determine the mean Zeeman factor as $364 \mu eV/T$. **b.** Temperature-dependent electron spin resonance measurements reveals a spin resonance at 335 mT, leading to an isotropic g -factor around 2.002, consistent with an isotropic triplet state⁵³. Inset: Goniometric electron spin resonance spectrum to determine isotropy of the spin states.

For an ensemble of defects, each of the hole spins in a singlet state has a different g -factor due to the different orientations in the lattice, leading to an additional inhomogeneous broadening of the PL spectrum under the magnetic field alongside the lifetime broadening, thermal broadening and the spectral diffusion between individual defect emissions. The resultant amplitude A of the spin-polarized photoluminescence has a Voigt-like profile that accounts for these effects, described by the below^{55,77}:

$$A(B_z, \Delta_f) = \int_{-\infty}^{\infty} \left(\frac{1}{\sigma_G \sqrt{2\pi}} e^{-\Delta_f^2 / 2\sigma_G^2} \right) \frac{\sigma_L / 2\pi}{(\sigma_L / 2)^2 + (\Delta_f - \epsilon_{eff} |B_z|)^2} d\Delta_f \quad (7)$$

Here, Δ_f is detuning, σ_G & σ_L are Gaussian-broadened and homogeneous linewidths, and ϵ_{eff} is the effective average Zeeman factor dependent on the hole g -factor variations. This leads to an approximate Voigt linewidth $\Gamma = \sqrt{((\Gamma_{B=0})^2 + (\epsilon_{eff} |B_z|)^2)}$ ⁵⁵.

To assess the possibility of a spin-photon interface, we measure the magnetic-field-induced broadening of the 0.56 meV-split doublet line using non-resonant photoluminescence spectroscopy under an out-of-plane DC magnetic field ranging from 0 mT to 500 mT at 4.5 K. Instrumental limitations, and the broadening induced by the natural-Si substrate does not allow us to distinguish the spin-degeneracy-lifted transitions within the ensemble fully, but Figure 5a shows the magnetic-field-induced broadening of the ensemble $^*Cu_n^m$ color center transitions. The intrinsic Voigt linewidth at 4.5 K and 0 mT is measured as 229 μeV for $^*Cu_0^0$ and measured as 235.9 μeV for $^*Cu_0^1$ line. While there is not a significant broadening observed for the $^*Cu_0^0$ line, a sizable linewidth increase is observed for the first excited state $^*Cu_0^0$, by 25% to 290 μeV . This increase in the linewidth is much larger than the instrument resolution. Using Eq.7, we extract the effective Zeeman factor ϵ_{eff} as 364 $\mu\text{eV/T}$ for the $^*Cu_0^0$ color center transition. Assuming that the novel doublet line is similar to T centers, we expect the formation of an unpaired hole-spin interacting with the ground-state electron within the first-excited transition of the $^*Cu_0^0$ -line. Further electron spin resonance analysis, which is given in Figure 5b, revealed that the ensembles of $^*Cu_0^0$ - $^*Cu_0^1$ defects provide a lambda-type spin-photon interface, with a degenerate ground level split with an isotropic g -factor of 2.002 and a Lorentzian broadening of 4 G, consistent with earlier observation for the isotropic triplet nature of the $^*Cu_0^0$ -peak⁵³. The ESR resonance signal around 335 mT shows a Gaussian-like broadening of 10 G above 10 K and disappears completely above 30 K, which is consistent with the thermalization of the $^*Cu_n^m$ PL lines. This further strengthens that the magnetic-field induced broadening in Figure 5a is due to the spin degeneracy of *Cu line.

III. CONCLUSION

In this study, we have examined the process steps leading to $^*Cu_n^m$ and T color centers' formation. During the T center formation process, we observe that the well-known G and W centers are already present after low-dose carbon implantation. Subsequently, we observe interestingly that the G and W centers disappear after the annealing process at 1000 $^\circ\text{C}$, only to be replaced by a doublet peak at 1312.15 nm ascribed as the $^*Cu_0^0$ and $^*Cu_0^1$ peaks, which are isoelectronic bound exciton peaks similar to T centers and originating from a Cu-Ag transition-metal color center. These optical transitions are present in the spectra of carbon implanted and annealed samples alongside the perturbed Cu-line phonon replicas. The Cu-line replicas between 1221.45 nm to 1238.64 nm and with 7 meV phonon energy are shown to confirm the predictions regarding the high electron-phonon coupling in W-centers. Furthermore, we have observed that the doublet $^*Cu_n^m$ optical transitions persist alongside TX₀ and TX₁ if the H_2O treatment is omitted and only RTA is applied to the sample. This doublet emission might lead to a novel spin-photon interface at O-band, and its magneto-optic properties will be examined further. We have examined and compared the TX₀ and TX₁ with $^*Cu_0^0$ and $^*Cu_0^1$ transitions and inves-

tigated their origins. The temperature-tuned μPL measurement showed that the $^*Cu_0^0$ and $^*Cu_0^1$ peaks result from lower and higher excited states transitions, respectively, of the same color centers whose formation induces a higher perturbation to the silicon host, compared to the less perturbative T centers, in-line with the presence of the W-line phonon replicas. We further estimate a much smaller exciton binding energy associated with this novel defect, down to 3.35 meV.

Based on the abovementioned process, we examined the bound exciton dynamics of the generated $^*Cu_n^m$ and T color centers. With time-resolved μPL measurements, we obtained radiative lifetimes of the $^*Cu_n^m$ transition at 52.4 ± 4.8 ns, and for the T center at 1.56 ± 0.13 μs , 65% longer than earlier studies²⁸. Compared to previous recipes, the gradual introduction of H atoms by H_2O treatment may help to have a sample devoid of all defects other than T centers. Reducing possible non-radiative decoherence pathways, as evidenced by extended lifetime, is of utmost importance for high-fidelity network nodes, while cavity QED interactions can increase the coherent photonic qubit emission rates. We have confirmed our experimental results by fitting the rate equation modeling between TX₀ and higher excited states, which leads to a slow carrier transition between TX₁ and TX₀, corresponding to the early-time slow-rising dynamics in our measured TRPL histograms. We further extracted the radiative and non-radiative recombination rates of the 3D confined T-center bound excitons.

The observed and improved T center lifetimes help to develop novel O-band quantum network nodes with high fidelity, involving cavity quantum electrodynamics of the spin-photon interface to control and route the emissions^{20,29}. The resolved $^*Cu_n^m$ doublet peak around 1312.15 nm offers a unique platform right at the zero-dispersion wavelengths in the O-band for qubit interactions. The determined excited-state radiative lifetimes magneto-optic and electron spin resonance measurements support the examinations of these silicon color centers towards solid-state quantum memories in scalable and metropolitan quantum networks.

IV. APPENDIX - EXPERIMENTAL SETUP

Power and temperature-dependent microphotoluminescence spectroscopy. A 532 nm solid-state continuous wave (CW) laser is used for the above-bandgap excitation with a continuous reflective neutral density (ND) filter for precise power control. A 925 nm dichroic mirror is used to reflect the incoming excitation laser to an objective (numerical aperture of 0.4) for focusing and PL collection. The samples are housed in a Lakeshore Janis ST-500 microscopy cryostat with a quartz window vertically set up. The collected PL is passed through the dichroic mirror and then a 905 nm long-pass filter to eliminate pump residual and directed into a Princeton Instruments 0.5-meter-long monochromator (SpectraPro 2500) with 600 g/mm grating. The magnetic-field-dependent measurements are done using room-temperature superconducting bore magnets with field intensities of 100, 200, 300, 400, and 500 mT. A liquid-nitrogen-cooled InGaAs camera is used to

measure individual lines with a spectral resolution of about 100 pm.

Time-resolved microphotoluminescence spectroscopy.—The μ PL spectroscopy setup is modified to utilize a pulse laser at 600 nm selected from a supercontinuum source (NKT Photonics SuperK Extreme) at a 2 MHz repetition rate, which creates a 40 μ m spot on the sample with an angle of about 45 degrees for side pumping. The focal points of the side excitation path and the collecting Mitutoyo objective are aligned by co-propagation from both beam paths. The collected light is passed through the same spectrometer with 1200 g/mm grating (spectral resolution \approx 40 pm) and directed to a photo-multiplier tube (PMT). The RF-synchronized signal and PMT output are connected to a Swabian Instruments (TimeTagger 20) time-to-digital converter, achieving an overall timing resolution of 400 ps.

V. ACKNOWLEDGEMENTS

The authors thank discussions with Joshua Pomeroy, Louis Bouchard, Madeline Taylor, and Kerry Kangdi Yu. The authors acknowledge support from the Army Research Office Multidisciplinary University Research Initiative (W911NF-21-2-0214), National Science Foundation under award numbers 2137984 (QuIC-TAQS) and 1936375 (QII-TAQS).

- ¹S. Wei, B. Jing, X. Zhang, J. Liao, C. Yuan, B. Fan, C. Lyu, D. Zhou, Y. Wang, G. Deng, H. Song, D. Oblak, G. Guo, and Q. Zhou, “Towards Real-World Quantum Networks: A Review,” *Laser & Photonics Reviews* **16**, 2100219 (2022).
- ²S. Ritter, C. Nölleke, C. Hahn, A. Reiserer, A. Neuzner, M. Uphoff, M. Mücke, E. Figueroa, J. Bochmann, and G. Rempe, “An elementary quantum network of single atoms in optical cavities,” *Nature* **484**, 195–200 (2012), 1202.5955.
- ³A. Reiserer and G. Rempe, “Cavity-based quantum networks with single atoms and optical photons,” *Reviews of Modern Physics* **87**, 1379–1418 (2015).
- ⁴G. Wolfowicz, F. J. Heremans, C. P. Anderson, S. Kanai, H. Seo, A. Gali, G. Galli, and D. D. Awschalom, “Quantum guidelines for solid-state spin defects,” *Nature Reviews Materials* **6**, 906–925 (2021).
- ⁵S. L. N. Hermans, M. Pompili, H. K. C. Beukers, S. Baier, J. Borregaard, and R. Hanson, “Qubit teleportation between non-neighbouring nodes in a quantum network,” *Nature* **605**, 663–668 (2022), 2110.11373.
- ⁶W. J. Munro, N. L. Piparo, J. Dias, M. Hanks, and K. Nemoto, “Designing tomorrow’s quantum internet,” *AVS Quantum Science* **4**, 020503 (2022).
- ⁷A. Reiserer, “Cavity-enhanced quantum network nodes,” *arXiv* (2022), 10.48550/arxiv.2205.15380, 2205.15380.
- ⁸M. K. Bhaskar, R. Riedinger, B. Machielse, D. S. Levonian, C. T. Nguyen, E. N. Knall, H. Park, D. Englund, M. Lončar, D. D. Sukachev, and M. D. Lukin, “Experimental demonstration of memory-enhanced quantum communication,” *Nature* **580**, 60–64 (2020), 1909.01323.
- ⁹W. Qin, A. Miranowicz, and F. Nori, “Proposal of ensemble qubits with two-atom decay,” *arXiv* (2023), 10.48550/arxiv.2302.06781, 2302.06781.
- ¹⁰N. Coste, D. Fioretto, N. Belabas, S. C. Wein, P. Hilaire, R. Frantzeskakis, M. Gündin, B. Goes, N. Somaschi, M. Morassi, A. Lemaître, J. Sagnes, A. Harouri, S. E. Economou, A. Auffèves, O. Krebs, L. Lanco, and P. Senellart, “High-rate entanglement between a semiconductor spin and indistinguishable photons,” (2022).
- ¹¹D. S. Levonian, R. Riedinger, B. Machielse, E. N. Knall, M. K. Bhaskar, C. M. Knaut, R. Bekenstein, H. Park, M. Lončar, and M. D. Lukin, “Optical Entanglement of Distinguishable Quantum Emitters,” *Physical Review Letters* **128**, 213602 (2022), 2108.10928.
- ¹²P.-J. Stas, Y. Q. Huan, B. Machielse, E. N. Knall, A. Suleymanzade, B. Pingault, M. Sutula, S. W. Ding, C. M. Knaut, D. R. Assumpcao, Y.-C. Wei, M. K. Bhaskar, R. Riedinger, D. D. Sukachev, H. Park, M. Lončar, D. S. Levonian, and M. D. Lukin, “Robust multi-qubit quantum network node with integrated error detection,” *Science* **378**, 557–560 (2022), 2207.13128.
- ¹³Y. Lei, F. K. Asadi, T. Zhong, A. Kuzmich, C. Simon, and M. Hosseini, “Quantum Optical Memory for Entanglement Distribution,” *arXiv* (2023), 10.48550/arxiv.2304.09397, 2304.09397.
- ¹⁴D. Cozzolino, B. D. Lio, D. Bacco, and L. K. Oxenløwe, “High-Dimensional Quantum Communication: Benefits, Progress, and Future Challenges,” *Advanced Quantum Technologies* **2**, 1900038 (2019), 1910.07220.
- ¹⁵M. Erhard, M. Krenn, and A. Zeilinger, “Advances in high-dimensional quantum entanglement,” *Nature Reviews Physics* **2**, 365–381 (2020), 1911.10006.
- ¹⁶K.-C. Chang, X. Cheng, M. C. Sarihan, A. K. Vinod, Y. S. Lee, T. Zhong, Y.-X. Gong, Z. Xie, J. H. Shapiro, F. N. C. Wong, and C. W. Wong, “648 Hilbert-space dimensionality in a biphoton frequency comb: entanglement of formation and Schmidt mode decomposition,” *npj Quantum Information* **7**, 48 (2021), 2005.07759.
- ¹⁷S. Yang, M. C. Sarihan, K.-C. Chang, C. W. Wong, and L. Dolecek, “Efficient Information Reconciliation for Energy-Time Entanglement Quantum Key Distribution,” 2019 53rd Asilomar Conference on Signals, Systems, and Computers **00**, 1364–1368 (2019).
- ¹⁸Y. Xiong, C. Bourgois, N. Sheremetyeva, W. Chen, D. Dahliah, H. Song, S. M. Griffin, A. Sipahigil, and G. Hautier, “High-throughput identification of spin-photon interfaces in silicon,” *arXiv* (2023), 2303.01594.
- ¹⁹I. R. Berkman, A. Lyasota, G. G. d. Boo, J. G. Bartholomew, S. Q. Lim, B. C. Johnson, J. C. McCallum, B.-B. Xu, S. Xie, N. V. Abrosimov, H.-J. Pohl, R. L. Ahlefeldt, M. J. Sellars, C. Yin, and S. Rogge, “Millisecond electron spin coherence time for erbium ions in silicon,” *arXiv* (2023), 10.48550/arxiv.2307.10021, 2307.10021.
- ²⁰A. Gritsch, A. Ulanowski, and A. Reiserer, “Purcell enhancement of single-photon emitters in silicon,” *Optica* **10**, 783 (2023), 2301.07753.
- ²¹A. N. Ramanayaka, K. Tang, J. A. Hagmann, H.-S. Kim, D. S. Simons, C. A. Richter, and J. M. Pomeroy, “Use of quantum effects as potential qualifying metrics for “quantum grade silicon,”” *AIP Advances* **9**, 125153 (2019).
- ²²K. Tang, H. S. Kim, A. N. Ramanayaka, D. S. Simons, and J. M. Pomeroy, “Targeted enrichment of 28Si thin films for quantum computing,” *Journal of Physics Communications* **4**, 035006 (2020).
- ²³K. J. Dwyer, J. M. Pomeroy, D. S. Simons, K. L. Steffens, and J. W. Lau, “Enriching 28Si beyond 99.9998 % for semiconductor quantum computing,” *Journal of Physics D: Applied Physics* **47**, 345105 (2014).
- ²⁴K. J. Dwyer, H. S. Kim, D. S. Simons, and J. M. Pomeroy, “Temperature-dependent Si29 incorporation during deposition of highly enriched Si28 films,” *Physical Review Materials* **1**, 064603 (2017).
- ²⁵K. Tang, H. S. Kim, A. N. R. Ramanayaka, D. S. Simons, and J. M. Pomeroy, “A compact, ultra-high vacuum ion source for isotopically enriching and depositing 28Si thin films,” *Review of Scientific Instruments* **90**, 083308 (2019).
- ²⁶K. Saeedi, S. Simmons, J. Z. Salvail, P. Dluhy, H. Riemann, N. V. Abrosimov, P. Becker, H.-J. Pohl, J. J. L. Morton, and M. L. W. Thewalt, “Room-temperature quantum bit storage exceeding 39 minutes using ionized donors in silicon-28,” *Science* **342**, 830–833 (2013), <https://www.science.org/doi/pdf/10.1126/science.1239584>.
- ²⁷K. J. Morse, R. J. S. Abraham, A. DeAbreu, C. Bowness, T. S. Richards, H. Riemann, N. V. Abrosimov, P. Becker, H.-J. Pohl, M. L. W. Thewalt, and S. Simmons, “A photonic platform for donor spin qubits in silicon,” *Science Advances* **3**, e1700930 (2017).
- ²⁸A. DeAbreu, C. Bowness, R. J. Abraham, A. Medvedova, K. J. Morse, H. Riemann, N. V. Abrosimov, P. Becker, H.-J. Pohl, M. L. W. Thewalt, and S. Simmons, “Characterization of the Si:Se+ Spin-Photon Interface,” *Physical Review Applied* **11**, 044036 (2019), 1809.10228.
- ²⁹W. Redjem, Y. Zhiyenbayev, W. Qarony, V. Ivanov, C. Papapanos, W. Liu, K. Jhuria, Z. Y. A. Balushi, S. Dhuey, A. Schwartzberg, L. Z. Tan, T. Schenkel, and B. Kanté, “All-silicon quantum light source by embedding an atomic emissive center in a nanophotonic cavity,” *Nature Communications* **14**, 3321 (2023), 2301.06654.
- ³⁰C. Beaufils, W. Redjem, E. Rousseau, V. Jacques, A. Y. Kuznetsov, C. Raynaud, C. Voisin, A. Benali, T. Herzig, S. Pezzagna, J. Meijer, M. Abbarchi, and G. Cassaboais, “Optical properties of an ensemble of G-centers in sili-

- con,” *Physical Review B* **97**, 035303 (2018), 1708.05238.
- ³¹W. Redjem, A. Durand, T. Herzig, A. Benali, S. Pezzagna, J. Meijer, A. Y. Kuznetsov, H. S. Nguyen, S. Cuffe, J.-M. Gerard, I. Robert-Philip, B. Gil, D. Caliste, P. Pochet, M. Abbarchi, V. Jacques, A. Dreau, and G. Cassaboïs, “Single artificial atoms in silicon emitting at telecom wavelengths,” *Nature Electronics* **3**, 738–743 (2020), 2001.02136.
 - ³²A. Durand, Y. Baron, W. Redjem, T. Herzig, A. Benali, S. Pezzagna, J. Meijer, A. Y. Kuznetsov, J.-M. Gerard, I. Robert-Philip, M. Abbarchi, V. Jacques, G. Cassaboïs, and A. Dreau, “Broad Diversity of Near-Infrared Single-Photon Emitters in Silicon,” *Physical Review Letters* **126**, 083602 (2021), 2010.11068.
 - ³³C.-W. Lee, M. Singh, A. C. Tamboli, and V. Stevanović, “Transition metal impurities in silicon: computational search for a semiconductor qubit,” *npj Computational Materials* **8**, 172 (2022), 2105.05927.
 - ³⁴Y. Xiong, C. Bourgeois, N. Sheremetyeva, W. Chen, D. Dahliah, H. Song, S. M. Griffin, A. Sipahigil, and G. Hautier, “High-throughput identification of spin-photon interfaces in silicon,” *arXiv* (2023), 2303.01594.
 - ³⁵W. Liu, V. Ivanov, K. Jhuria, Q. Ji, A. Persaud, W. Redjem, J. Simoni, Y. Zhiyenbayev, B. Kante, J. G. Lopez, L. Z. Tan, and T. Schenkel, “Quantum Emitter Formation Dynamics and Probing of Radiation-Induced Atomic Disorder in Silicon,” *Physical Review Applied* **20**, 014058 (2023).
 - ³⁶Y. Baron, A. Durand, P. Udvarhelyi, T. Herzig, M. Khoury, S. Pezzagna, J. Meijer, I. Robert-Philip, M. Abbarchi, J.-M. Hartmann, V. Mazzocchi, J.-M. Gerard, A. Gali, V. Jacques, G. Cassaboïs, and A. Dreau, “Detection of Single W-Centers in Silicon,” *ACS Photonics* **9**, 2337–2345 (2022), 2108.04283.
 - ³⁷M. Hollenbach, N. Klingner, N. S. Jagtap, L. Bischoff, C. Fowley, U. Kentsch, G. Hlawacek, A. Erbe, N. V. Abrosimov, M. Helm, Y. Berencén, and G. V. Astakhov, “Wafer-scale nanofabrication of telecom single-photon emitters in silicon,” *Nature Communications* **13**, 7683 (2022), 2204.13173.
 - ³⁸V. Saggio, C. Errando-Herranz, S. Gyger, C. Panuski, M. Prabhu, L. D. Santis, I. Christen, D. Ornelas-Huerta, H. Raniwala, C. Gerlach, M. Colangelo, and D. Englund, “Cavity-enhanced single artificial atoms in silicon,” *arXiv* (2023), 10.48550/arxiv.2302.10230, 2302.10230.
 - ³⁹B. Lefaucher, J.-B. Jager, V. Calvo, A. Durand, Y. Baron, F. Cache, V. Jacques, I. Robert-Philip, G. Cassaboïs, T. Herzig, J. Meijer, S. Pezzagna, M. Khoury, M. Abbarchi, A. Dreau, and J.-M. Gerard, “Cavity-enhanced zero-phonon emission from an ensemble of G centers in a silicon-on-insulator microring,” *Applied Physics Letters* **122**, 061109 (2023), 2210.05485.
 - ⁴⁰C. Chartrand, L. Bergeron, K. J. Morse, H. Riemann, N. V. Abrosimov, P. Becker, H.-J. Pohl, S. Simmons, and M. L. W. Thewalt, “Highly enriched Si28 reveals remarkable optical linewidths and fine structure for well-known damage centers,” *Physical Review B* **98**, 195201 (2018), 1807.10718.
 - ⁴¹L. Bergeron, C. Chartrand, A. T. K. Kurkjian, K. J. Morse, H. Riemann, N. V. Abrosimov, P. Becker, H. J. Pohl, M. L. W. Thewalt, and S. Simmons, “Silicon-Integrated Telecommunications Photon-Spin Interface,” *PRX Quantum* **1** (2020), 10.1103/prxquantum.1.020301, 2006.08793.
 - ⁴²A. DeAbreu, C. Bowness, A. Alizadeh, C. Chartrand, N. A. Brunelle, E. R. MacQuarrie, N. R. Lee-Hone, M. Ruether, M. Kazemi, A. T. K. Kurkjian, S. Roorda, N. V. Abrosimov, H.-J. Pohl, M. L. W. Thewalt, D. B. Higginbottom, and S. Simmons, “Waveguide-integrated silicon t centres,” *Opt. Express* **31**, 15045–15057 (2023).
 - ⁴³D. B. Higginbottom, F. K. Asadi, C. Chartrand, J.-W. Ji, L. Bergeron, M. L. Thewalt, C. Simon, and S. Simmons, “Memory and transduction prospects for silicon t center devices,” *PRX Quantum* **4**, 020308 (2023).
 - ⁴⁴M. C. Sarihan, J. Huang, W. Liu, J. H. Kang, B. Liang, and C. W. Wong, “Cryogenic O-band photoluminescence spectroscopy of T-centers in monolithic Si for mesoscopic cavity quantum electrodynamics,” *Conference on Lasers and Electro-Optics*, JTu3B.36 (2022).
 - ⁴⁵C. Fan, M. C. Sarihan, J. Huang, K. M. Azizur-Rahman, J. H. Kang, B. Liang, W. Liu, and C. W. Wong, “Cryogenic optical spectroscopy of color-centers in Si for quantum information processing,” *CLEO 2023*, JTh2A.8 (2023).
 - ⁴⁶J. Huang, M. C. Sarihan, J. H. Kang, B. Liang, W. Liu, and C. W. Wong, “Cryogenic optical transitions of T centers in bulk Silicon and Silicon-on-insulator for cavity quantum electrodynamics,” *Frontiers in Optics + Laser Science* 2021, JTu7A.2 (2021).
 - ⁴⁷A. N. Safonov, E. C. Lightowers, G. Davies, P. Leary, R. Jones, and S. Öberg, “Interstitial-Carbon Hydrogen Interaction in Silicon,” *Physical Review Letters* **77**, 4812–4815 (1996).
 - ⁴⁸L. Song, X. Zhan, B. Benson, and G. Watkins, “Bistable interstitial-carbon–substitutional-carbon pair in silicon,” *Physical Review B* **42**, 5765 (1990).
 - ⁴⁹M. Steger, A. Yang, N. Stavrias, M. L. W. Thewalt, H. Riemann, N. V. Abrosimov, M. F. Churbanov, A. V. Gusev, A. D. Bulanov, I. D. Kovalev, A. K. Kaliteevskii, O. N. Godisov, P. Becker, and H.-J. Pohl, “Reduction of the Linewidths of Deep Luminescence Centers in Si28 Reveals Fingerprints of the Isotope Constituents,” *Physical Review Letters* **100**, 177402 (2008).
 - ⁵⁰M. Steger, A. Yang, T. Sekiguchi, K. Saeedi, M. L. W. Thewalt, M. O. Henry, K. Johnston, H. Riemann, N. V. Abrosimov, M. F. Churbanov, A. V. Gusev, A. K. Kaliteevskii, O. N. Godisov, P. Becker, and H.-J. Pohl, “Photoluminescence of deep defects involving transition metals in Si: New insights from highly enriched 28Si,” *Journal of Applied Physics* **110**, 081301 (2011).
 - ⁵¹N. Q. Vinh, J. Phillips, G. Davies, and T. Gregorkiewicz, “Time-resolved free-electron laser spectroscopy of a copper isoelectronic center in silicon,” *Physical Review B* **71**, 085206 (2004).
 - ⁵²K. McGuigan, M. Henry, E. Lightowers, A. Steele, and M. Thewalt, “A new photoluminescence band in silicon lightly doped with copper,” *Solid State Communications* **68**, 7–11 (1988).
 - ⁵³K. McGuigan, M. Henry, M. Carmo, G. Davies, and E. Lightowers, “A uniaxial stress study of a copper-related photoluminescence band in silicon,” *Materials Science and Engineering: B* **4**, 269–272 (1989).
 - ⁵⁴D. B. Higginbottom, A. T. K. Kurkjian, C. Chartrand, M. Kazemi, N. A. Brunelle, E. R. MacQuarrie, J. R. Klein, N. R. Lee-Hone, J. Stacho, M. Ruether, C. Bowness, L. Bergeron, A. DeAbreu, S. R. Harrigan, J. Kananayagam, D. W. Marsden, T. S. Richards, L. A. Stott, S. Roorda, K. J. Morse, M. L. W. Thewalt, and S. Simmons, “Optical observation of single spins in silicon,” *Nature* **607**, 266–270 (2022).
 - ⁵⁵E. R. MacQuarrie, C. Chartrand, D. B. Higginbottom, K. J. Morse, V. A. Karasyuk, S. Roorda, and S. Simmons, “Generating T centres in photonic silicon-on-insulator material by ion implantation,” *New Journal of Physics* **23**, 103008 (2021).
 - ⁵⁶J. F. Ziegler, M. Ziegler, and J. Biersack, “SRIM – The stopping and range of ions in matter,” *Nuclear Instruments and Methods in Physics Research Section B: Beam Interactions with Materials and Atoms* **268**, 1818–1823 (2010), 19th International Conference on Ion Beam Analysis.
 - ⁵⁷A. Henry, B. Monemar, J. L. Lindström, T. D. Bestwick, and G. O. S. Hehrlein, “Photoluminescence characterization of plasma exposed silicon surfaces,” *Journal of Applied Physics* **70**, 5597–5603 (1991).
 - ⁵⁸I. Santos, M. Aboy, P. López, L. A. Marqués, and L. Pelaz, “Insights on the atomistic origin of X and W photoluminescence lines in c-Si from ab initio simulations,” *Journal of Physics D: Applied Physics* **49**, 075109 (2016).
 - ⁵⁹V. Ivanov, J. Simoni, Y. Lee, W. Liu, K. Jhuria, W. Redjem, Y. Zhiyenbayev, C. Papapanos, W. Qarony, B. Kanté, A. Persaud, T. Schenkel, and L. Z. Tan, “Effect of localization on photoluminescence and zero-field splitting of silicon color centers,” *Phys. Rev. B* **106**, 134107 (2022).
 - ⁶⁰Y. Baron, A. Durand, P. Udvarhelyi, T. Herzig, M. Khoury, S. Pezzagna, J. Meijer, I. Robert-Philip, M. Abbarchi, J.-M. Hartmann, V. Mazzocchi, J.-M. Gerard, A. Gali, V. Jacques, G. Cassaboïs, and A. Dreau, “Detection of Single W-Centers in Silicon,” *ACS Photonics* **9**, 2337–2345 (2022), 2108.04283.
 - ⁶¹S. Cherkova, V. Skuratov, and V. Volodin, “Luminescence properties of FZ silicon irradiated with swift heavy ions,” *Semiconductors* **53**, 1427–1430 (2019).
 - ⁶²G. Davies, E. Lightowers, and Z. E. Ciechanowska, “The 1018 meV (W or I1) vibronic band in silicon,” *Journal of Physics C: Solid State Physics* **20**, 191 (1987).
 - ⁶³S. Estreicher and A. Carvalho, “The CuPL defect and the Cus1Cui3 complex,” *Physica B: Condensed Matter* **407**, 2967–2969 (2012).
 - ⁶⁴T. Fujimura and K. Shirai, “Revisiting the stable structure of the Cu4 complex in silicon,” *Japanese Journal of Applied Physics* **60**, 021001 (2021), 1912.11586.
 - ⁶⁵S. Estreicher and A. Carvalho, “The CuPL defect and the Cus1Cui3 complex,” *Physica B: Condensed Matter* **407**, 2967–2969 (2012).
 - ⁶⁶T. M. Vincent and S. K. Estreicher, “Ag and Ag–Cu interactions in Si,” *Journal of Applied Physics* **128**, 155703 (2020).

- ⁶⁷T. Schenkel, W. Redjem, A. Persaud, W. Liu, P. A. Seidl, A. J. Amsellem, B. Kanté, and Q. Ji, "Exploration of defect dynamics and color center qubit synthesis with pulsed ion beams," *Quantum Beam Science* **6** (2022), 10.3390/qbs6010013.
- ⁶⁸K. Thonke, H. Klemisch, J. Weber, and R. Sauer, "New model of the irradiation-induced 0.97-eV (G) line in silicon: A C S- Si* complex," *Physical Review B* **24**, 5874 (1981).
- ⁶⁹J. Gower, G. Davies, E. C. Lightowlers, and A. Safonov, "The I centre: A hydrogen related defect in silicon," in *Materials Science Forum*, Vol. 258 (Trans Tech Publ, 1997) pp. 289–294.
- ⁷⁰R. Pässler, "Parameter sets due to fittings of the temperature dependencies of fundamental bandgaps in semiconductors," *Physica Status Solidi (B)* **216**, 975–1007 (1999).
- ⁷¹M. Cardona and M. L. Thewalt, "Isotope effects on the optical spectra of semiconductors," *Reviews of Modern Physics* **77**, 1173 (2005).
- ⁷²E. Irion, N. Burger, K. Thonke, and R. Sauer, "The defect luminescence spectrum at 0.9351 eV in carbon-doped heat-treated or irradiated silicon," *Journal of Physics C: Solid State Physics* **18**, 5069 (1985).
- ⁷³T. Sjödin, H. Petek, and H.-L. Dai, "Ultrafast carrier dynamics in silicon: A two-color transient reflection grating study on a (111) surface," *Physical Review Letters* **81**, 5664 (1998).
- ⁷⁴M. Wörle, A. W. Holleitner, R. Kienberger, and H. Iglev, "Ultrafast hot-carrier relaxation in silicon monitored by phase-resolved transient absorption spectroscopy," *Physical Review B* **104**, L041201 (2021).
- ⁷⁵D. Dhaliya, Y. Xiong, A. Sipahigil, S. M. Griffin, and G. Hautier, "First-principles study of the T center in silicon," *Physical Review Materials* **6**, L053201 (2022).
- ⁷⁶D. Rosales, T. Bretagnon, B. Gil, A. Kahouli, J. Brault, B. Damilano, J. Massies, M. V. Durnev, and A. V. Kavokin, "Excitons in nitride heterostructures: From zero- to one-dimensional behavior," *Physical Review B* **88**, 125437 (2013).
- ⁷⁷B. H. McGuyer, M. McDonald, G. Z. Iwata, M. G. Tarallo, W. Skomorowski, R. Moszynski, and T. Zelevinsky, "Precise study of asymptotic physics with subradiant ultracold molecules," *Nature Physics* **11**, 32–36 (2015).